Determination of Electron Band Structure using Temporal Interferometry

Liang Li,[1] Pengfei Lan,[1,*] Lixin He,[1] Wei Cao,[1] Qingbin Zhang,[1] and Peixiang Lu[1,2,3,†]

[1]*Wuhan National Laboratory for Optoelectronics and School of Physics, Huazhong University of Science and Technology, Wuhan 430074, China*

[2]*Hubei Key Laboratory of Optical Information and Pattern Recognition, Wuhan Institute of Technology, Wuhan 430205, China*

[3]*CAS Center for Excellence in Ultraintense Laser Science, Shanghai 201800, China*

(Received 11 June 2019; revised manuscript received 14 August 2019; accepted 31 March 2020; published 16 April 2020)

We propose an all-optical method to directly reconstruct the band structure of semiconductors. Our scheme is based on the temporal Young's interferometer realized by high harmonic generation with a few-cycle laser pulse. As a time-energy domain interferometer, temporal interference encodes the band structure into the fringe in the energy domain. The relation between the band structure and the emitted harmonic frequencies is established. This enables us to retrieve the band structure from the spectrum of high harmonic generation with a single-shot measurement. Our scheme paves the way to study matters under ambient conditions and to track the ultrafast modification of band structures.

DOI: 10.1103/PhysRevLett.124.157403

The electron band structure can be understood as the material fingerprint in the reciprocal space and determines many properties of materials. Measuring the band structure is of great importance for understanding the properties of materials. Usually, the electron band structure of solids is mapped by independently measuring the momentum and the energy of incoherent electrons by the angle-resolved photoemission spectroscopy (ARPES) [1]. Normally, only the sample area close to the surface can be investigated, because the electron mean free paths in solids are typically in the angstrom scale. In addition, the photoelectrons are sometimes difficult or impossible to be detected because of the scattering by ambient conditions [2].

In recent years, high harmonic generation (HHG) has been observed experimentally from a wide variety of solid media [3–9], from general semiconductors to novel materials such as graphene. This opens an avenue toward attosecond science on the platform of solid-state materials [10–14] and suggests new approaches for crystallographic analysis and probing the electronic properties of solids [15–19]. Different from the traditional electronic techniques, the method based on HHG measures the high harmonic photons. This all-optical method has high temporal resolution, making it possible to study the ultrafast transient modifications of band structures. Very recently, several works [20–22] propose to measure the band structure of ZnO and ZnSe by HHG. In their methods, the harmonic spectra are detected as a function of the field intensity or the time delay between the two-color field. Then, the band structure is retrieved by comparing the measured harmonic yields with those calculated from a set of trial bands, and finding the one that best fits the experiments. These methods, however, rely on the calculations of high harmonic spectra with numerical models and the reconstructions are partially based on the theoretical simulations or assumptions. The band reconstruction is very time consuming. It sometimes becomes even computationally prohibitive to get a convergent retrieval when the number of undetermined parameters becomes large. Moreover, these methods need multishot measurements to obtain the intensity (or delay) dependent high harmonic yields. It prevents one from effectively capturing the band structure and realizing the time-resolved measurements of ultrafast dynamics.

In this Letter, we demonstrate a method to directly reconstruct the band structure. Our scheme is based on the generalized temporal Young's interferometer [23–25]. As illustrated in Fig. 1, we construct a temporal two-slit with a few cycle laser field. The HHG is dominantly contributed to by two emissions, because the ionization is constrained within an optical cycle near the peak of the envelope. Two representative trajectories (red and blue lines in Fig. 1) propagate oppositely at two sequent half cycles accompanied with harmonics emissions at different times (the middle line of Fig. 1). The interference fringe comes from these two emissions, i.e., the peaks of the HHG spectrum are very sensitive to the phase difference in the wave front between the two slits, which is encoded by the band structure. Then, one can directly retrieve the band structure by monitoring the interference fringe.

To show how one can retrieve the band structure from the HHG signal, we first explain the concept of temporal interferometry. By dividing the wave function into two parts $|\Psi(t)\rangle = |\Psi_g(t)\rangle + |\Psi_e(t)\rangle$, where $|\Psi_g(t)\rangle$ is the field free ground part, and $|\Psi_e(t)\rangle$ is the field induced excited part, we can rewrite the time-dependent Schrödinger equation (TDSE) as [26],

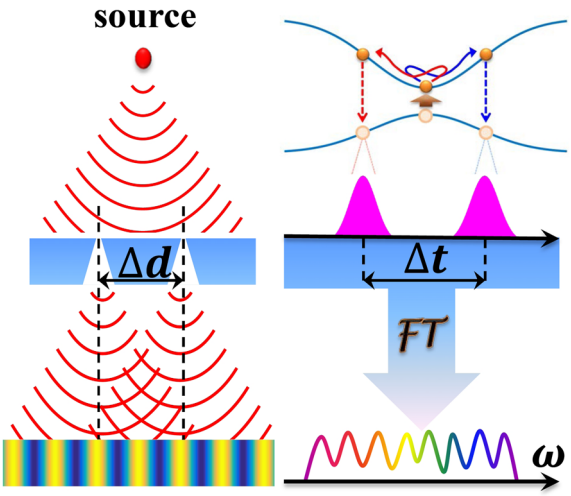

FIG. 1. The sketch of the two-slit interferometer of HHG in solids. The graph on the left shows a typical two slit interference. The graph on the right shows the time-domain interference in HHG. An electron source is generated at the top of the valence band and two bursts are emitted at the two adjacent half laser cycles. These two bursts construct a two-slit interferometer and the interference fringes will be observed in the frequency domain.

$$\left[i\frac{\partial}{\partial t}-\hat{H}_{\text{free}}-\hat{H}_{\text{int}}\right]|\Psi_{g,\mathbf{k}_0}(t)\rangle=\hat{H}_{\text{int}}|\Psi_{e,\mathbf{k}_0}(t)\rangle, \quad (1)$$

where $\hat{H}_{\text{free}}$ is the field free Hamiltonian and $\hat{H}_{\text{int}}$ is the interaction Hamiltonian. The generated high harmonic can be expressed by a series of emissions in time domain [27,28],

$$P(\Omega,t)=\sum_{t',t_r,\mathbf{k}_0}^{m,n} a_{mn}(t',t_r,\mathbf{k}_0)e^{-iS_{mn}(t',t_r,\mathbf{k}_0)}\mathbf{p}_{mn}(t',t_r,\mathbf{k}_0), \quad (2)$$

where $\mathbf{k}_0$ is the crystal momentum for the electron, and m, n are the band indexes. The parameter $t', t_r, \mathbf{k}_0$ can be obtained from the saddle point equation. $a_{mn}(t',t_r,\mathbf{k}_0)$ is the weight of the channel and $\mathbf{p}_{mn}(t',t_r,\mathbf{k}_0)$ is the polarization between the electron-hole pairs when recollision occurs. The intraband terms are not shown because with the parameters used in this work the high harmonics beyond the minimum band gap are mainly contributed by the interband terms. Typical semiconductors exhibit band structure with multiple valence and conduction bands. However, in many cases, coupling between multiple bands is expected to be negligible for wide separated bands, or even closely spaced bands of similar symmetry. As shown in previous works [21,22,30,31], the signal of the target bands can be identified from the multivalence and multiconduction bands under appropriate laser parameters. Then, one can retrieve the band gap $E_m - E_n$ by using the temporal interferometry.

To demonstrate our scheme, we perform the simulated experiment with ZnO. The same band dispersion $E_m(\mathbf{k}) = E_{m,x}(k_x) + E_{m,y}(k_y) + E_{m,z}(k_z)$ as that in Refs. [21,32,33] is used. The orientation of the reciprocal lattice is chosen so that $\hat{x}\|\Gamma - M$, $\hat{y}\|\Gamma - K$, and $\hat{z}\|\Gamma - A$ (optical axis). The laser field is propagating along the optical axis $\hat{z}$. We adopt a Gaussian envelope and the electric field can be expressed as

$$\mathbf{F}(t)=\hat{x}F_0 e^{-2ln2(t/\tau)^2}\cos(\omega t+\phi); \quad (3)$$

ω and ϕ are the frequency and carrier-envelope phase (CEP) of the laser field, respectively. The wavelength and the intensity of the laser field are 3 μm ($\omega = 0.015$ a.u.) and 9×10^{11} W/cm^2 ($F_0 = 0.005$ a.u.), respectively. Atomic units (a.u.) are applied throughout this Letter unless stated. A few-cycle laser pulse with $\tau = 1.5T_0$ is used, where $T_0 = (2\pi/\omega)$ is an optical cycle (o.c.). Because of the restriction of the few-cycle pulse, only two trajectories at the pulse peak are dominant, which construct a two-slit separated approximately by half optical cycle. The high harmonic spectra can be obtained from the semiconductor Bloch equation (SBE) [32,34,35]

$$\begin{aligned}
&\frac{d\pi(\mathbf{K},t)}{dt}=-\frac{\pi(\mathbf{K},t)}{T_2}-i\xi(\mathbf{K},t)[2N_v(\mathbf{K},t)-1]e^{-iS(\mathbf{K},t)},\\
&\frac{dN_v(\mathbf{K},t)}{dt}=-i\xi^*(\mathbf{K},t)\pi(\mathbf{K},t)e^{iS(\mathbf{K},t)}+\text{c.c.},\\
&\frac{d[N_v(\mathbf{K},t)+N_c(\mathbf{K},t)]}{dt}=0,
\end{aligned} \quad (4)$$

where N_m ($m = c,\ v$) is the band population. $S(\mathbf{K},t) = \int_{t_0}^{t}\{E_c[\mathbf{K}+\mathbf{A}(t')]-E_v[\mathbf{K}+\mathbf{A}(t')]\}dt'$ is the classical action, $\xi(\mathbf{K},t) = \mathbf{F}(t)\cdot\mathbf{d}[\mathbf{K}+\mathbf{A}(t)]$ is the Rabi frequency, and $\mathbf{d}(\mathbf{k}) = \mathbf{d}^*_{cv}(\mathbf{k}) = \mathbf{d}_{vc}(\mathbf{k}) = \langle c,\mathbf{k}|\hat{\mathbf{r}}|v,\mathbf{k}\rangle$ is the transition dipole moment with $|m,\mathbf{k}\rangle$ representing the Bloch states. $\mathbf{K} = \mathbf{k} - \mathbf{A}(t)$ is the shifted crystal momentum with the vector potential $[d\mathbf{A}(t)/dt] = -\mathbf{F}(t)$, and the first Brillouin zone is also shifted to $\bar{\text{BZ}} = \text{BZ} - \mathbf{A}(t)$. T_2 is a dephasing-time term describing the coherence between the conduction and valence bands. We choose $T_2 = 2.5$ fs in the simulation. The numerical value of dipole moment at the Γ point, $\mathbf{d}_{cv} = (3.46, 3.46, 3.94)$, is applied. As in Refs. [32,35,36], the k dependence of the dipole moment is neglected. For computational convenience, we perform the two-dimensional (2D) calculations (i.e., $k_z = 0$ in reciprocal space). The reciprocal space is discretized by a grid with 481×481 points. By numerically solving the SBE, one can obtain the intraband $\mathbf{J}_{ra}$ and interband $\mathbf{J}_{er}$ currents as follows,

$$\mathbf{J}_{ra}(t)=\sum_{m=c,v}\int_{\bar{\text{BZ}}}\mathbf{v}_m[\mathbf{k}+\mathbf{A}(t)]n_m(\mathbf{K},t)d^3\mathbf{K}, \quad (5)$$

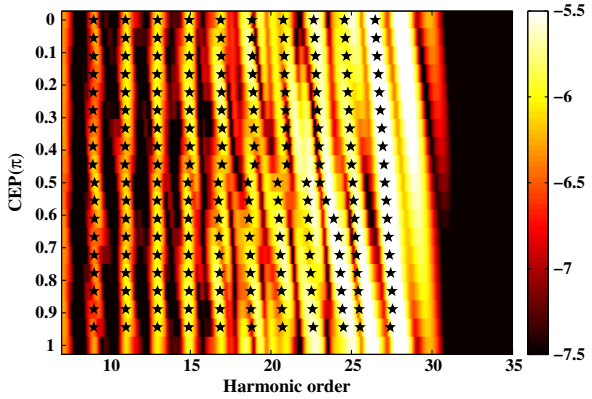

FIG. 2. The harmonic spectra for different CEP. The stars mark the results obtained with the two-slit interferometer.

$$\mathbf{J}_{er}(t) = \frac{d}{dt}\int_{\mathrm{BZ}} \mathbf{d}[\mathbf{k}+\mathbf{A}(t)]\pi(\mathbf{K},t)e^{iS(\mathbf{K},t)}d^3\mathbf{K} + \mathrm{c.c.}, \quad (6)$$

where $\mathbf{v}_m(\mathbf{k}) = \nabla_{\mathbf{k}} E_m(\mathbf{k})$ is the group velocity in band m. High harmonic spectra are obtained from the Fourier transform of these currents. As discussed above, we only consider the interband current in this work.

Figure 2 shows the HHG spectra with the CEP changing from 0 to π. The harmonic order is identified by the frequency of the laser field, and the harmonics with photon energy lower than the minimum band gap are not shown. As shown in Fig. 2, the harmonic peaks are deviated from the odd harmonics [$O_n = (2n-1)\omega$], which are expected with a multicycle driven laser. For $\phi = 0$, the harmonic peaks are redshifted compared to the odd harmonics. With the increase of the harmonic order, the frequency shift becomes more and more evident. When the CEP changes from 0 to 0.5π, the harmonic peaks shift to higher photon energy, and even become blueshifted compared to the odd harmonics. When the CEP changes from 0.5 to 1π, the harmonic peaks show similar structure to those from 0 to 0.5π.

To quantitatively understand the above results, we show the time-frequency spectrogram of HHG in Fig. 3(a). Only the signal near the pulse center is shown, because the signal outside this region is relatively weaker and will not influence the discussion. As shown in Fig. 3(a), there are two dominant emissions, which are contributed by the electrons ionized at adjacent half cycles at the center of the few-cycle pulse. We choose two representative emissions with the same energy, which are referred to as "1" and "2" in Fig. 3(b). These two emissions construct a temporal two-slit interferometer. The interference can be described by $d(t) = d(t-t_1) + d(t-t_2)e^{i(\pi+\Delta S)}$. Here $\Delta t = t_2 - t_1$ is the slit gap and $\Delta S = S_2 - S_1$ is the phase difference between the channels 1 and 2. Note that π phase shift is due to the reversal sign of the electric field. The slit gap and phase difference vary with the emitted photon energy. As a

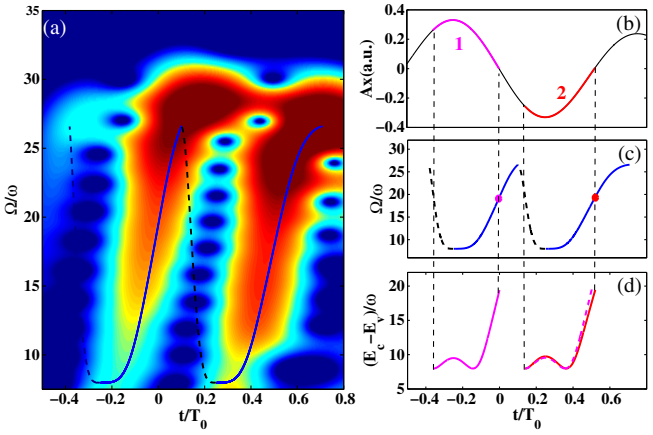

FIG. 3. (a) Time-frequency spectrogram for $\phi = 0$. (b) The vector potential of the electric field. 1 and 2 mark two typical channels for an identical photon energy. (c) The emission energy versus the ionization time and the emission time obtained with Eq. (8). (d) The paths of 1 and 2 in the energy domain.

time-energy domain interferometry, fringes in the energy domain are expressed as $I(\Omega) \propto |1 + e^{i[\Omega*\Delta t+\Delta S+\pi]}|^2$. We have ignored the amplitude difference of these two emissions. Then we can obtain the constructive interference, i.e., the peak in the HHG spectrum,

$$\Omega = \left(\frac{T_0}{2\Delta t}\right) O_n - \Delta S/\Delta t. \quad (7)$$

The displacement of the interference fringe, that is, the frequency shift between the harmonic peaks and the original odd harmonics $\Delta\omega = \Omega - O_n$ is then expressed as $\Delta\omega = [(T_0/2\Delta t) - 1]O_n - \Delta S/\Delta t$. There are two terms contributed to the frequency shift. The first is originated from the deviation of slit gap Δt compared with $T_0/2$. It is proportional to the harmonic energy. The second term is originated from the phase difference ΔS between the trajectories through two slits, and its influence is modulated by the slit gap. Note that, in Eq. (7) we do not include the influence of the transition dipole phase. It works well for a crystal with reflection symmetry along the polarization direction of the laser field. For the crystals without reflection symmetry, both the band structure and the transition dipole phase will influence the HHG spectrum [39–41]. In this case, an additional measurement is required in our method to retrieve both the transition dipole phase and the band structure [see Sec. F in the Supplemental Material (SM) [28]].

By analyzing the quantum trajectories, one can obtain the slit gap Δt and the phase different ΔS in the two-slit interferometer. Considering the acceleration theorem and the energy conservation, the relation between the photon energy and emission time can be obtained according to the saddle point equations [36–38]:

$$\int_{t_i}^{t} \partial_{k_x} E_c[-Ax(t_i)+Ax(t')] - \partial_{k_x} E_v[-Ax(t_i)+Ax(t')]dt' = 0,$$
$$E_c[-Ax(t_i)+Ax(t)] - E_v[-Ax(t_i)+Ax(t)] = \Omega. \quad (8)$$

Here, we assume a minimal direct band gap at the Γ point. The lines in Figs. 3(a) and 3(c) show the results predicted with Eqs. (8). The blue solid lines show the photon energy as a function of emission time and the dashed black lines show the photon energy as a function of ionization time. The phase accumulated by the electron through different paths can be expressed as $S_i = \int_{t_i}^{tr_i}\{E_c[-Ax(t_i)+Ax(t')]-E_v[-Ax(t_i)+Ax(t')]\}dt'$, where t_i and tr_i are the ionization time and emission time, respectively. In Fig. 3(d), we show the trajectories 1 (pink solid line) and 2 (red solid line) in the energy domain. The pink dashed line is a copy of trajectory 1 moved by Δt. One can see that the trajectories are modulated in adjacent half cycles, which leads to a phase difference between two emissions. The time delay Δt (solid red line) and the phase difference ΔS (dashed red line) between two emissions are shown in Fig. 4(a). One can see that these two emissions are not separated by exactly half cycle. Instead, the time delay between these two emissions, i.e., the slit gap Δt, gradually increases with the increase of photon energy. In contrast, the phase difference ΔS gradually decreases.

According to Eq. (7), slit gaps larger than $T_0/2$ will give rise to a redshift while negative phase difference will give rise to blueshift comparing to the odd harmonics. With the slit gaps and the phases differences, one can obtain the interference fringe. The results for CEP $\phi = 0$ are shown as dashed black lines in Fig. 4(b). One can see a larger redshift for the higher harmonics, which can be attributed to the bigger slit gaps [see Fig. 4(a)]. By changing the CEP, two channels will move under an overall envelope, which leads to different slit gaps Δt and phase differences ΔS. Following the same procedure as we do in Fig. 4, the CEP dependence of the constructive interference peaks can be obtained. As shown by the stars in Fig. 2, the prediction of the two-slit interferometer agrees very well with the SBE simulations. The slight discrepancy between the two-slit interference and the simulation is induced by an additional emission that emerges with increasing the CEP (see details in Sec. B in the Supplemental Material [28]).

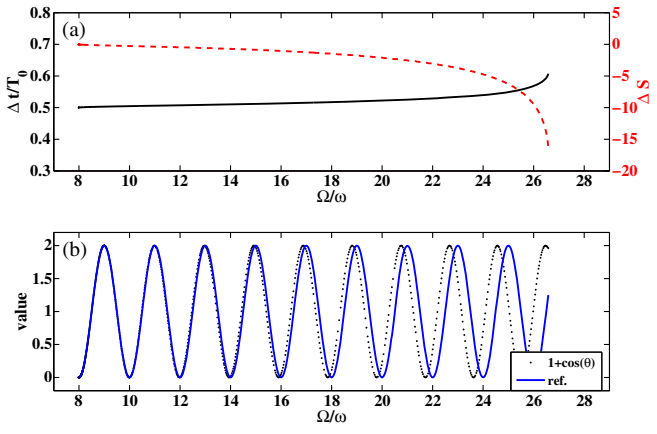

FIG. 4. (a) The time delay Δt (solid black line) and the phase difference ΔS (dashed red line) versus photon energy. (b) Interference fringe of the two-slit interferometer (solid black line) and the reference fringe (solid blue line) with $\Delta t = T_0/2$ and $\Delta S = 0$. The CEP is 0.

Next, we discuss how to retrieve the band structure from the interference fringe, i.e., the peaks Ω in the HHG spectrum. We refer to the frequency of the harmonic in the simulated experiment as $H_{\phi,n}$ for a given CEP, e.g., $\phi = 0$. As in Ref. [22], we expand the band gap with the Fourier series,

$$\epsilon(k_x, \mathbf{c}) = \epsilon_g + \sum_{s=1}^{5} c_s \cos(s k_x a_x). \quad (9)$$

We assume a known minimum band gap ϵ_g, which can be accurately measured with linear optical methods. Then, the above equation has 5 independent parameters $\mathbf{c} = \{c_1, c_2, c_3, c_4, c_5\}$. Ten points from the simulated experiment are used, i.e., the circles in Fig. 5(a), which are well enough to determine a band structure with 5 independent parameters. The parameters $\mathbf{c}$ can be obtained by using a self-consistent iterative method (see details in Sec. C of the Supplemental Material [28]). Our iterative method is more efficient than the best fitting algorithm, especially when the parameter space becomes larger. Moreover, our reconstruction is based on the temporal interferometer, without calculating the harmonic spectra as a function of laser parameters. Therefore, the band structure can be determined by a single-shot measurement. The single-shot measurement can be easily combined with the pump-probe scheme, which facilitates tracking the modification of band structure in real time. The time resolution is about the pulse duration of the few-cycle pulse (~10 fs), which is fast enough for lots of processes in semiconductors.

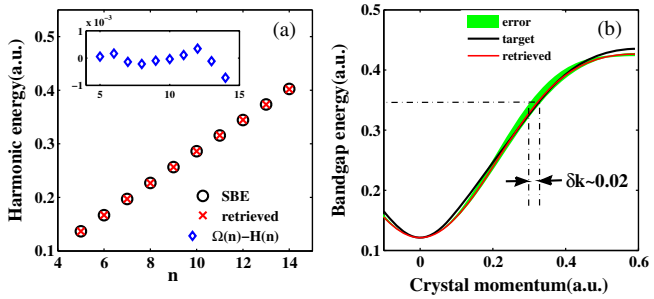

FIG. 5. (a) The retrieved harmonic's frequencies and the results simulated with SBE. For clarity, the difference between the simulation and retrieved results is shown in the inset. (b) The target and retrieved band structure.

Figure 5(a) shows the retrieved harmonic's frequencies. The difference is less than 10^{-3} compared to the simulated experiment. Figure 5(b) shows the retrieved (red line) band structures obtained from the simulated experiment with $\phi = 0$. One can see that the retrieved band structure well reproduces the target band (black line) with only a small difference near the maximum band energy. The deviation mainly originates from the relatively lower cutoff energy of the saddle point. As shown in Fig. 5(a), the highest energy is about 0.40 a.u. In that case, the simulated result can not give an accuracy band data near the maximum band energy 0.44 a.u. We also reconstruct the band structure by using the simulated experiment with different ϕ. The retrieved band structures also lie very close to the target (see details in Sec. D of the Supplemental Material [28]). In realistic experiments, there are always some uncertainties in the laser parameters. To evaluate this influence, we consider that the fluctuations of the laser intensity and CEP are $\pm 5\%$ and ± 50 mrad, respectively. Under these conditions, the uncertainty of the reconstruction is shown in Fig. 5(b) with the green shadow curves. The momentum resolution amounts to $\delta k \sim 0.02$ a.u.

In conclusion, we present a temporal Young's interferometer and demonstrate its applications for retrieving the band structure of ZnO. In our scheme, the reconstruction is based on the relation between the frequency shift and the modulation of the time slits. By monitoring the frequency shift of HHG in a few cycle laser field, we can directly retrieve the band structure of ZnO by a single-shot measurement. This time-energy domain interferometry method is anticipated to possess advantageous time resolving capability. The high temporal resolution and all-optical single-shot measurement make it suitable to study matters under ambient conditions and it paves the way to track the ultrafast processes with the pump-probe approach.

This work was supported by National Natural Science Foundation (NSFC) of China (Grants No. 91950202, No. 11934006, No. 11627809, No. 11874165), National Key Research and Development Program (2017YFE0116600).

*pengfeilan@hust.edu.cn
†lupeixiang@hust.edu.cn

[1] A. Damascelli, Z. Hussain, and Z. X. Shen, Rev. Mod. Phys. **75**, 473 (2003).
[2] A. M. Shuvaev, V. Dziom, N. N. Mikhailov, Z. D. Kvon, Y. Shao, D. N. Basov, and A. Pimenov, Phys. Rev. B **96**, 155434 (2017).
[3] S. Ghimire, A. D. DiChiara, E. Sistrunk, P. Agostini, L. F. DiMauro, and D. A. Reis, Nat. Phys. **7**, 138 (2011).
[4] G. Vampa, T. J. Hammong, N. Thiré, B. E. Schmidt, F. Légaré, C. R. McDonald, T. Brabec, and P. B. Corkum, Nature (London) **522**, 462 (2015).
[5] M. Hohenleutner, F. Langer, O. Schubert, M. Knorr, U. Huttner, S. W. Koch, M. Kira, and R. Huber, Nature (London) **523**, 572 (2015).
[6] Y. S. You, Y. Yin, Y. Wu, A. Chew, X. Ren, F. Zhuang, S. Gholam-Mirzaei, M. Chini, Z. Chang, and S. Ghimire, Nat. Commun. **8**, 724 (2017).
[7] N. Yoshikawa, T. Tamaya, and K. Tanaka, Science **356**, 736 (2017).
[8] Y. Murakami, M. Eckstein, and P. Werner, Phys. Rev. Lett. **121**, 057405 (2018).
[9] R. A. Ganeev *et al.*, Opt. Express **26**, 35013 (2018).
[10] A. Schiffrin *et al.*, Nature (London) **493**, 70 (2013).
[11] M. Schultze *et al.*, Nature (London) **493**, 75 (2013).
[12] B. Zaks, R. B. Liu, and M. S. Sherwin, Nature (London) **483**, 580 (2012).
[13] F. Langer *et al.*, Nature (London) **533**, 225 (2016).
[14] F. Langer *et al.*, Nature (London) **557**, 76 (2018).
[15] A. von Hoegen, R. Mankowsky, M. Fechner, M. Först, and A. Cavalleri, Nature (London) **555**, 79 (2018).
[16] T. T. Luu and H. J. Wörner, Nat. Commun. **9**, 916 (2018).
[17] H. B. Banks, Q. Wu, D. C. Valovcin, S. Mack, A. C. Gossard, L. Pfeiffer, R. B. Liu, and M. S. Sherwin, Phys. Rev. X **7**, 041042 (2017).
[18] C. Yu, S. Jiang, T. Wu, G. Yuan, Z. Wang, C. Jin, and R. Lu, Phys. Rev. B **98**, 085439 (2018).
[19] C. Wang, Tak-San Ho, and Shih-I Chu, J. Phys. B **49**, 225401 (2016).
[20] T. T. Luu, M. Garg, S. Yu, A. Moulet, M. Th. Hassan, and E. Goulielmakis, Nature (London) **521**, 498 (2015).
[21] G. Vampa, T. J. Hammond, N. Thire, B. E. Schmidt, F. Legare, C. R. McDonald, T. Brabec, D. D. Klug, and P. B. Corkum, Phys. Rev. Lett. **115**, 193603 (2015).
[22] A. A. Lanin, E. A. Stepanov, A. B. Fedotov, and A. M. Zheltikov, Optica **4**, 516 (2017).
[23] W. K. Wootters and W. H. Zurek, Phys. Rev. D **19**, 473 (1979).
[24] M. O. Scully, B.-G. Englert, and H. Walther, Nature (London) **351**, 111 (1991).
[25] Y. S. You *et al.*, Opt. Lett. **42**, 1816 (2017).
[26] W. Becker and M. Kleber, Phys. Scr. **94**, 023001 (2019).
[27] L. Li, P. Lan, X. Zhu, T. Huang, Q. Zhang, M. Lein, and P. Lu, Phys. Rev. Lett. **122**, 193901 (2019).
[28] See Supplemental Material at http://link.aps.org/supplemental/10.1103/PhysRevLett.124.157403 for additional discussions of the results and details of the iterative algorithm, which includes Ref. [29].
[29] G. Vampa and T. Brabec, J. Phys. B **50**, 083001 (2017).
[30] M. Wu, S. Ghimire, D. A. Reis, K. J. Schafer, and M. B. Gaarde, Phys. Rev. A **91**, 043839 (2015).
[31] C. R. McDonald, G. Vampa, P. B. Corkum, and T. Brabec, Phys. Rev. A **92**, 033845 (2015).
[32] G. Vampa, C. R. McDonald, G. Orlando, D. D. Klug, P. B. Corkum, and T. Brabec, Phys. Rev. Lett. **113**, 073901 (2014).
[33] M. Goano, F. Bertazzi, M. Penna, and E. Bellotti, J. Appl. Phys. **102**, 083709 (2007).
[34] D. Golde, T. Meier, and S. W. Koch, Phys. Rev. B **77**, 075330 (2008).
[35] T. T. Luu and H. J. Wörner, Phys. Rev. B **94**, 115164 (2016).

[36] G. Vampa, C. R. McDonald, G. Orlando, P. B. Corkum, and T. Brabec, Phys. Rev. B **91**, 064302 (2015).
[37] T. Ikemachi, Y. Shinohara, T. Sato, J. Yumoto, M. Kuwata-Gonokami, and K. L. Ishikawa, Phys. Rev. A **95**, 043416 (2017).
[38] S. Jiang, C. Yu, G. Yuan, T. Wu, Z. Wang, and R. Lu, J. Phys. Condens. Matter **29**, 275702 (2017).
[39] S. Jiang, H. Wei, J. Chen, C. Yu, R. Lu, and C. D. Lin, Phys. Rev. A **96**, 053850 (2017).
[40] S. Jiang, J. Chen, H. Wei, C. Yu, R. Lu, and C. D. Lin, Phys. Rev. Lett. **120**, 253201 (2018).
[41] C. Yu, X. Zhang, S. Jiang, X. Cao, G. Yuan, T. Wu, L. Bai, and R. Lu, Phys. Rev. A **94**, 013846 (2016).